



RESEARCH ARTICLE

Quantitative neuroimaging measures of myelin in the healthy brain and in multiple sclerosis

Jonathan O'Muircheartaigh^{1,2,3,4}  | Irene Vavasour⁵ | Emil Ljungberg³  |
David K. B. Li^{5,6} | Alexander Rauscher^{5,7,8} | Victoria Levesque⁹ | Hideki Garren⁹ |
David Clayton⁹ | Roger Tam^{5,6,10} | Anthony Traboulsee^{6,11} | Shannon Kolind^{5,6,7,11}

¹Department of Forensic and Neurodevelopmental Sciences, Institute of Psychiatry Psychology and Neuroscience, King's College London, London, United Kingdom

²Centre for the Developing Brain, Department of Perinatal Imaging and Health, St. Thomas' Hospital, King's College London, London, United Kingdom

³Department of Neuroimaging, Institute of Psychiatry Psychology and Neuroscience, King's College London, London, United Kingdom

⁴MRC Centre for Neurodevelopmental Disorders, King's College London, London, United Kingdom

⁵Department of Radiology, University of British Columbia, Vancouver, British Columbia, Canada

⁶MS/MRI Research Group, Djavad Mowafaghian Centre for Brain Health, University of British Columbia, Vancouver, British Columbia, Canada

⁷Department of Physics and Astronomy, University of British Columbia, Vancouver, British Columbia, Canada

⁸Department of Pediatrics, University of British Columbia, Vancouver, British Columbia, Canada

⁹Genentech, Inc., South San Francisco, California

¹⁰School of Biomedical Engineering, University of British Columbia, Vancouver, British Columbia, Canada

¹¹Division of Neurology, Department of Medicine, University of British Columbia, Vancouver, British Columbia, Canada

Correspondence

Shannon Kolind, Department of Medicine,
University of British Columbia, S-199 UBC
Hospital, 2211 Wesbrook Mall, Vancouver,
British Columbia V6T2B5, Canada.
Email: shannon.kolind@ubc.ca

Abstract

Quantitative magnetic resonance imaging (MRI) techniques have been developed as imaging biomarkers, aiming to improve the specificity of MRI to underlying pathology compared to conventional weighted MRI. For assessing the integrity of white matter (WM), myelin, in particular, several techniques have been proposed and investigated individually. However, comparisons between these methods are lacking. In this study, we compared four established myelin-sensitive MRI techniques in 56 patients with relapsing–remitting multiple sclerosis (MS) and 38 healthy controls. We used T2-relaxation with combined GRAdient And Spin Echoes (GRASE) to measure myelin water fraction (MWF-G), multi-component driven equilibrium single pulse observation of T₁ and T₂ (mcDESPOT) to measure MWF-D, magnetization-transfer imaging to measure magnetization-transfer ratio (MTR), and T₁ relaxation to measure quantitative T₁ (qT₁). Using voxelwise Spearman correlations, we tested the correspondence of methods throughout the brain. All four methods showed associations that varied across tissue types; the highest correlations were found between MWF-D and qT₁ (median ρ across tissue classes 0.8) and MWF-G and MWF-D (median ρ = 0.59). In eight WM tracts, all measures showed differences ($p < 0.05$) between MS normal-appearing WM and healthy control WM, with qT₁ showing the highest number of different regions (8), followed by MWF-D and MTR (6), and MWF-G ($n = 4$). Comparing the methods in terms of their statistical sensitivity to MS lesions in WM, MWF-D demonstrated the best accuracy ($p < 0.05$, after multiple comparison correction). To aid future power analysis, we provide the average and standard deviation volumes of the four techniques, estimated from the healthy control sample.

Jonathan O'Muircheartaigh and Irene Vavasour contributed equally to this study.

This is an open access article under the terms of the Creative Commons Attribution License, which permits use, distribution and reproduction in any medium, provided the original work is properly cited.

© 2019 The Authors. *Human Brain Mapping* published by Wiley Periodicals, Inc.

KEYWORDS

individual differences, magnetization transfer ratio, multiple sclerosis, myelin, myelin water imaging, quantitative MRI, relaxometry

1 | INTRODUCTION

Quantitative magnetic resonance imaging (MRI) techniques that are used as markers of white matter (WM) and myelin content include magnetic resonance relaxation-based and magnetization transfer-based methods. Both approaches provide WM *contrast* related to myelin, but are predicated on different assumptions and models, and may not directly correspond to each other (Alexander et al., 2011; De Santis, Drakesmith, Bells, Assaf, & Jones, 2014). Diseases of WM, and multiple sclerosis (MS) in particular have motivated the search for quantitative and specific MRI measures of myelin content as measures of treatment response and remission (Filippi et al., 2012). Although conventional clinical MRI protocols for monitoring MS include qualitative T_1 and T_2 weighted images, these lack specificity to the underlying pathology and are difficult to compare across imaging sites and scanners (Barkhof, Calabresi, Miller, & Reingold, 2009). Quantitative MRI can supplement standard clinical imaging by providing detection of changes within normal appearing tissue, as well as biological characterization of these alterations (MacKay and Laule, 2016).

Multicomponent relaxation-based techniques model tissue water compartments by observing the difference in relaxation times. For example, water trapped between myelin bilayers and the water inside or outside of axons have different T_1 and T_2 relaxation times, and by measuring the relative signal contribution from each component, a measure such as the myelin water fraction (MWF) can be obtained (Deoni, Rutt, Arun, Pierpaoli, & Jones, 2008; MacKay et al., 2006). The MWF is positively correlated with myelin content, and therefore lower MWF is thought to reflect a decrease in myelin content (Laule et al., 2008). Quantification of the macromolecular content as a proxy for myelin can be performed using the magnetization transfer ratio (MTR; Filippi et al., 1995; Schmierer, Scaravilli, Altmann, Barker, & Miller, 2004), the more advanced quantitative magnetization transfer (qMT; Schmierer et al., 2007), or the macromolecular tissue volume (MTV; Mezer et al., 2013). A decrease in MTR is commonly interpreted as a decrease of myelin. T_1 -relaxation time (commonly referred to as quantitative T_1 , qT_1) is also found in the literature as a quantitative biomarker for pathology (Margaret Cheng, Stikov, Ghugre, & Wright, 2012), with increased qT_1 associated with myelin loss.

Many of these techniques have been investigated in MS (Harrison et al., 2013; Kitzler et al., 2012; Kolind et al., 2012; Ontaneda, Thompson, Fox, & Cohen, 2016). For multi-echo techniques, Laule et al. (2006, 2008) demonstrated strong associations across tissue types between histological staining of myelin and the T_2 -relaxation-based MWF obtained with a multi-echo spin echo sequence. The acquisition can be achieved in clinically feasible times using a combined Gradient And Spin Echo (GRASE) sequence (Prasloski et al., 2012); the MWF measurement obtained using a GRASE is here termed MWF-G. An alternative, and more recently, multicomponent relaxation technique is mcDESPOT, from which the fraction of signal attributed to myelin water (here called MWF-D), similar to MWF-G, can be obtained. To

date, there is no human *ex vivo* histology validation of mcDESPOT. However, Hurley et al. (2010) used the shaking pup preclinical model of dysmyelination and showed that MWF-D was sensitive, at the very least, to an absence of myelin. Wood et al. (2016) performed whole-brain mcDESPOT in a cuprizone mouse model and found a decrease in MWF-D, related to the expected demyelination. MTR has been validated against postmortem tissue using histopathology, showing good sensitivity to myelin and demyelination (Schmierer et al., 2004). However, since MTR measures the interaction between macromolecular protons and bulk water, it is also related to the total water content of tissue and therefore, in cases of WM injury, edema, and inflammation can obscure the myelin-related signal (Gareau, Rutt, Karlik, & Mitchell, 2000; Vavasour, Laule, Li, Traboulsee, & MacKay, 2011). In addition, some postmortem studies have found an even larger association between MTR and axonal count (Mottershead et al., 2003; Van Waesberghe et al., 1999). Single component measures of qT_1 have also been shown to correlate strongly with histological staining for myelin (Schmierer et al., 2007). However, interpretations of changes in T_1 are confounded by the known relationship between $1/T_1$ and $1/\text{water content}$ (Fatouros, Marmarou, Kraft, Inao, & Schwarz, 1991; Gelman, Ewing, Gorell, Spickler, & Solomon, 2001; Kamman, Go, Brouwer, & Berendsen, 1988; Rooney et al., 2007). Thus, it is difficult to deduce whether changes in T_1 are due to demyelination and/or changes in total water content.

The common feature of most of these validation studies is that they have shown that the quantitative image *contrast* is similar between myelin-sensitive techniques, though they do not correspond only to the amount of myelin present. Even histological stains, such as luxol fast blue, provide a *contrast*; the optical density of these contrasts does not in itself provide a quantification of tissue content (Stüber et al., 2014). In general, strong correlations *across* tissue types (in the brain typically white and gray matter) indicate that two methods have similar tissue contrast, an important precondition. However, the level of consistency between quantities from the different methods is unclear.

In this study, we investigated the cross-subject similarity between four prominent quantitative MRI techniques that are associated with WM content: Multi-echo T_2 relaxation, mcDESPOT, MTR, and qT_1 . The techniques were compared against each other to determine which technique best separates tissue between MS patients and healthy controls. Finally, we investigated the relative sensitivity of each of these techniques to lesional WM in individual patients with MS.

2 | METHODS

2.1 | Participants

The study cohort consisted of 56 patients with relapsing–remitting MS (19:37 male:female; mean age = 37 years, range = 20–55; median

TABLE 1 Overview of the study cohort

	MS patients (N = 56)	MS patients subset* (N = 24)	Healthy controls (N = 38)
Age (years)	Mean: 37 Range 20–55	Mean: 37 Range 20–53	Mean: 35, range: 20–53
Sex	19 M, 37 F	9 M, 15 F	13 M, 25 F
EDSS	Median: 2.0 Range: 0–4.0	Median: 2.0 Range: 0–4.0	
Lesion volume (mm ³)	Mean: 7394, median: 3523, range: 446–47,370	Mean: 4031, median: 2327, range: 214–14,047	
Number of lesions (count)	Mean: 26.5, median: 22.5, range: 3–71	Mean: 33, median: 30.5, range: 3–71	

*Only patients with all 4 quantitative imaging techniques collected.

EDSS = 2.0, EDSS range = 0.0–4.0) recruited as part of a clinical trial of ocrelizumab versus interferon beta 1a (OPERA II; NCT01412333) (Hauser et al., 2017), and 38 age and gender-matched healthy controls (13 male; mean age = 34, range = 20–53). As described in Hauser et al. (2017), to be eligible to take part in the study, MS patients were required to have at least two undocumented clinical relapses within the previous 2 years or one clinical relapse in the year before screening. MRI data needed to show MS consistent abnormalities and no neurological worsening over the 30 days prior to screening. In addition, participants were excluded if they had a disease duration of over 10 years.

Data presented here were acquired at baseline, prior to the initiation of treatment. Details of the patient and control cohort are presented in Table 1. Thirty-two MS patients did not have an MTR scan due to time constraints, thus 24 of the 56 patients had all four MRI techniques acquired (MS Patients Subset in Table 1). This subset of 24 was used when comparing imaging methods in the MS group only. This study was approved by the University of British Columbia Clinical Research Ethics Board and all subjects provided written informed consent before participating in the study.

2.2 | MRI data acquisition

All MR imaging was performed on a Philips 3T Achieva scanner (Best, The Netherlands) using an eight-channel head RF array coil. For localization, a true midline sagittal scan (TR = 1900 ms, TI = 800 ms, TE = 10 ms) and a quick T₂-weighted scan (TR = 2,792 ms, TE = 90 ms, 60 axial slices acquired at 3 mm slice thickness, in-plane voxel size = 1 × 1 mm², field of view [FOV] = 250 × 188 × 180 mm³) were performed. A 3D-T1-weighted gradient echo scan (TR = 28 ms, TE = 4 ms, 60 axial slices acquired at 3 mm slice thickness, in-plane voxel size = 1 × 1 mm², flip angle = 27°, FOV = 250 × 188 × 180 mm³) was also acquired. For lesion identification, a proton density weighted (PDw) (TR = 2000 ms, TE = 10 ms, 60 axial slices acquired at 3 mm slice thickness, in-plane voxel size = 1 × 1 mm², FOV = 250 × 200 × 180 mm³, echo train length [ETL] = 3), a T₂-weighted (TR = 6,100 ms, TE = 80 ms, 60 axial slices acquired at 3 mm slice thickness, in-plane voxel size = 1 × 1 mm², FOV = 250 × 188 × 180 mm³, ETL = 8), and a FLAIR (TR = 9,000 ms, TE = 80 ms, TI = 2,500 ms, 60 axial slices acquired at 3 mm slice thickness, in-plane voxel size = 1 × 1 mm², FOV = 250 × 188 × 180 mm³, ETL = 12) sequence were collected. Table 2 summarizes all pulse sequence parameters.

2.3 | Quantitative imaging sequences

2.3.1 | GRASE

Multi-echo T₂ relaxation was measured using a GRASE sequence (TR = 1,000 ms, TE = 10 ms, ETL = 32, 20 axial slices acquired at 5 mm slice thickness and reconstructed to 40 slices at 2.5 mm slice thickness, slice oversampling factor = 1.3, in-plane voxel size = 1 × 1 mm², FOV = 230 × 192 × 100 mm³, EPI factor = 3) (Prasloski, Rauscher, et al., 2012).

2.3.2 | mcDESPOT

The mcDESPOT protocol was composed of a series of sagittally oriented spoiled gradient recalled echo (SPGR) and balanced steady-state free precession (bSSFP) acquisitions across a range of flip angles (α) as well as an inversion-recovery-prepared SPGR (IR-SPGR) scan for correction of flip angle inhomogeneity (Deoni, 2011). A common isotropic voxel size of 1.7 × 1.7 × 1.7 mm³ and field of view of 220 × 160 × 220 mm³ were used for all images. Scan parameters for the individual sequences were: SPGR: TR = 6.5 ms; TE = 3.6 ms; α = [2, 3, 4, 6, 9, 13, 18]°, bSSFP: TR = 5.8 ms; TE = 2.9 ms; α = [7, 11, 15, 19, 24, 30, 47]°, IRSPGR: TR = 6.5 ms; TE = 3.2 ms; α = 5°; TI = 450 ms; for the bSSFP volumes, all flip angles were acquired with phase-cycling patterns of 0° and 180° for correction of off-resonance effects (Deoni, 2011).

2.3.3 | Magnetization transfer imaging

The magnetization transfer imaging acquisition consisted of a 3D gradient echo sequence (TR = 85 ms, TE = 3.7 ms, 20 axial slices acquired at 5 mm slice thickness and reconstructed to 40 slices at 2.5 mm slice thickness, in-plane voxel size = 1 × 1 mm², FOV = 230 × 192 × 100 mm³, α = 18°, with and without an off-resonance RF pulse centered 1.1 kHz below the water frequency, sinc-gaussian envelope of duration = 15 ms, bandwidth = 190 Hz, amplitude = 2.3 × 10⁻⁶ T).

2.4 | Quantitative image processing

The signal decay curve obtained by the GRASE T₂ relaxation sequence was modeled by multiple exponential components and the T₂ distribution was estimated using nonnegative least squares with the extended phase graph algorithm as well as spatial regularization (Prasloski, Mädler, Xiang, MacKay, & Jones, 2012; Whittall & MacKay, 1989; Yoo et al., 2015). The MWF-G was calculated in each image voxel as the ratio of the area under the T₂ distribution with 10 ≤ T₂ ≤ 40 ms

TABLE 2 MRI sequence pulse sequence parameters

	Quick T2	3DT1	PD lesion	T2 lesion	FLAIR	GRASE	mcDESPOT			MTR
							SPGR	bSSFP	IRSPGR	
Resolution acquired/ reconstructed [mm ²]	1 × 1.2/1 × 1	1 × 1/1 × 1	1 × 1/1 × 1	1 × 1/1 × 1	1 × 1	1 × 1	1.7 × 1.7	1.7 × 1.7	1.7 × 1.7	1 × 1
Slice thickness acquired/ reconstructed [mm]	3/3	3/3	3/3	3/3	3/3	5/2.5	1.7/1.7	1.7/1.7	3.4/1.7	5
Number of reconstructed slices	60	60	60	60	60	40	92	92	92	20
Field of view (FOV)	250 × 188 × 180	250 × 188 × 180	250 × 200 × 180	250 × 188 × 180	250 × 188 × 180	230 × 192 × 100	220 × 160 × 220	220 × 160 × 220	220 × 160 × 220	230 × 192 × 100
Echo time (TE) [ms]	90	4	10	80	80	10	3.6	2.9	3.2	3.7
Repetition time (TR) [ms]	2,792	28	2000	6,100	9,000	1,000	6.5	5.8	6.5	85
Inversion time (TI) [ms]	n/a	n/a	n/a	n/a	2,500	n/a	n/a	n/a	450	n/a
Flip angle (α) [deg]	120 ^a	27	n/a	n/a	120 ^a	180 ^a	2, 3, 4, 6, 9, 13, 18	7, 11, 15, 19, 24, 30, 47	5	18
Echo train length (ETL)	22	n/a	3	8	12	32	n/a	n/a	n/a	n/a
Scan mode	MS	3D	MS	MS	MS	3D	3D	3D	3D	3D
Parallel imaging (SENSE)	No	No	No	No	No	2 (RL)	2 (AP)	2 (AP)	2 (AP)	2 (RL)
Partial k-space	No	No	No	No	No	No	0.6	0.6	No	0.6
Acquisition time [min]	2	5:3	4:5	4:9	7:2	14:5	3 ^b	2:7 ^b	1:1	3:5

MS, Multislice (2D); RL, right-left; AP, anterior-posterior; n/a, not applicable.

^a Refocusing flip angle.^b Total acquisition time for all flip angles.

to the total area under the distribution. From the mcDESPOT data, the MWF-D and qT_1 maps were calculated using the processing methods outlined in Deoni and Kolind (2015); briefly, the SPGR and IR-SPGR scans were used for DESPOT1 with High-speed Incorporation of RF Field Inhomogeneities (DESPOT1-HIFI) analysis (Deoni, 2007), resulting in maps of the global T_1 and the B_1 field. The bSSFP data (acquired with two phase-cycling schemes) and the global T_1 and B_1 maps were then used to calculate global T_2 and B_0 field maps using DESPOT2 with full modeling (DESPOT2-FM) analysis (Deoni, 2009). Finally, the B_0 and B_1 maps combined with the SPGR and bSSFP (with both phase-cycling schemes) were used to calculate the MWF using stochastic region contraction (Deoni & Kolind, 2015). MTR maps were created by calculating $(M_0 - M_s)/M_0 \times 100$ for each voxel, where M_0 is the image without the saturation pulse and M_s is the image with the saturation pulse.

2.5 | Registration to template space

To provide a representative common space for the datasets collected here, a study-specific template was constructed, from the high flip angle (18°) T_1w SPGR image of 40 subjects. This was performed using

the ANTs package (version 2.1.x; <https://github.com/stnava/ANTs>) and implemented using the *buildtemplateparallel.sh* script (Avants et al., 2011). We chose the high flip angle T_1w image as it has good gray/WM tissue contrast and has isotropic resolution whereas the 3D gradient echo T_1w image had nonisotropic voxels. This template was built from an age-matched subgroup of the subjects with and without MS (40 images in total, 10 male and 10 female per group, with an average age of 36). A final nonlinear transformation was calculated from this template space to MNI space, also using the ANTs package.

Within-subject, MTR (image without the saturation pulse), MWF-G (first echo GRASE image), and PDw images were registered to the high flip-angle T_1w -weighted SPGR images from the mcDESPOT sequence using rigid registration (FLIRT; Jenkinson & Smith, 2001). For each subject, this T_1w image was then nonlinearly registered to the study-specific template (ANTs; Avants, Epstein, Grossman, & Gee, 2008). Finally, using the combined registrations, the MWF-G, MWF-D, qT_1 , and MTR quantitative maps were registered and resampled into 1 mm isotropic MNI space in a single linear interpolation step. In addition, for the patient sample, the lesion masks (which are described below) were registered and resampled into MNI space using nearest neighbor interpolation. The registration pipeline is outlined in Figure 1.

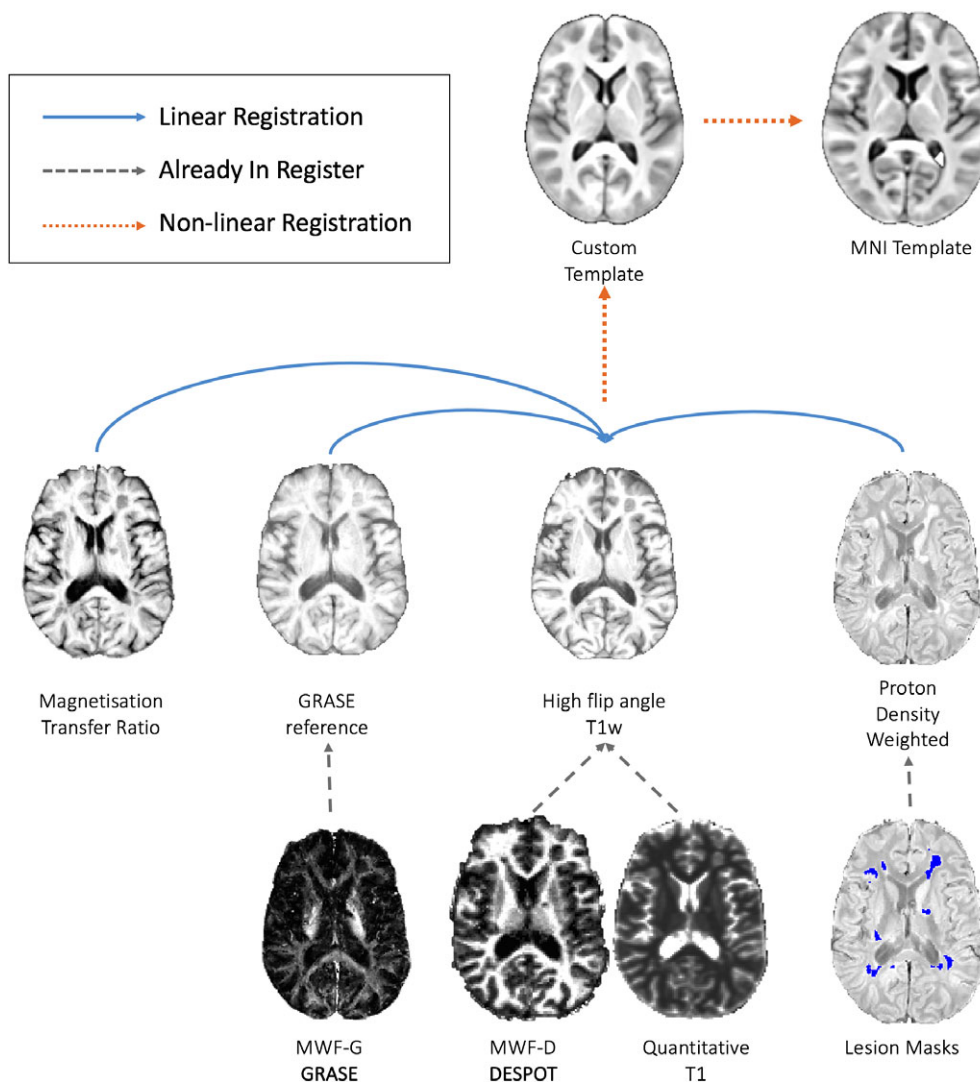


FIGURE 1 Registration pipeline for resampling all images to a common template [Color figure can be viewed at wileyonlinelibrary.com]

2.6 | Delineation of lesion and regions of interest

Lesions were identified on the T_2w , PDw, and FLAIR for each subject by an experienced radiologist, placing one or more seed points where a lesion was identified. Segmentation was then performed automatically using the provided seed points according to the method described by Tam, Traboulsee, Riddehough, Sheikhzadeh, and Li (2011) and McAusland et al. (2010). In addition to the semi-automatically defined lesions masks, additional masks of the boundary of each lesion (2 mm dilation of the semi-automatically defined lesion) were created and are referred to here as peri-lesional tissue.

Tissue masks were derived from the Harvard–Oxford atlas distributed as part of the FSL package (<https://fsl.fmrib.ox.ac.uk/fsl>). Three masks were created, one for gray matter, one for WM, and one encompassing subcortical structures (amygdala, hippocampus, basal ganglia, and thalamus; Figure 3). Anatomical regions of interest in WM were defined in standard space using the JHU probabilistic tractography atlas (Hua et al., 2008). These regions were then combined with the group WM tissue mask to ensure only WM was included. Eight major WM bundles were investigated: anterior thalamic radiation (ATR), cingulum, cortico-spinal tract (CSP), forceps major, forceps minor, inferior fronto-occipital fasciculus (IFO), inferior longitudinal fasciculus (ILF), and superior longitudinal fasciculus (SLF). For patients, the tissue and WM regions of interest excluded both the lesion and perilesional tissue, thus full brain WM segmentation is referred to as normal-appearing WM (NAWM).

2.7 | Summary and correlation maps

A group average quantitative map and a standard deviation (SD) map were created for each modality from the healthy control group. Spearman correlation maps between the different quantitative values at every voxel were calculated for the whole brain using 3dTcorrelate, part of the AFNI package (Cox, 1996). Correlation maps and histograms (per tissue class) of the correlation coefficients were produced.

2.8 | Receiver operator characteristic maps

For all quantitative data sets available in the patient population, individual-patient voxelwise difference maps were created by Z-normalizing the patient's parameter maps to the mean and SD of the healthy control sample. In the 24 patients for whom all four quantitative sequences were successfully acquired (see Table 1 for characteristics), receiver operator characteristic (ROC) curves were constructed for each individual dataset, testing the accuracy of each MRI method for lesional WM detection (Fawcett, 2006). These curves were generated by using a range of Z-score cutoffs between the minimum and maximum Z-score and comparing whether each voxel was inside or outside of the Z-score cutoff and whether the same voxel was included or not included within the semi-automated lesion masks. For every threshold, the proportion of voxels outside of the Z-score cutoff (considered to be lesional from the advanced MR technique) that were also inside the semi-automated lesion mask is equal to the true positive rate. The percentage of voxels above the Z-score cutoff but outside of the semi-automated lesion mask is equal to the false positive rate. To compare the sensitivity/specificity of the four methods to manually defined lesions, the area under the curve (AUC) of ROCs from each dataset was calculated for each subject and compared pairwise across all methods using a nonparametric Friedman test. Post hoc inter-method comparisons were tested using Wilcoxon tests (Demšar, 2006), corrected for multiple comparisons using the Bonferroni–Holm step-down method.

3 | RESULTS

Sample mean and SD maps of the 38 healthy control datasets are illustrated in Figure 2. In all four methods, the SD values are lower in WM than in gray matter, reflecting the fact that these are healthy adult controls (so no large deviations in WM content are expected). All analyses comparing methods or including the patient group were

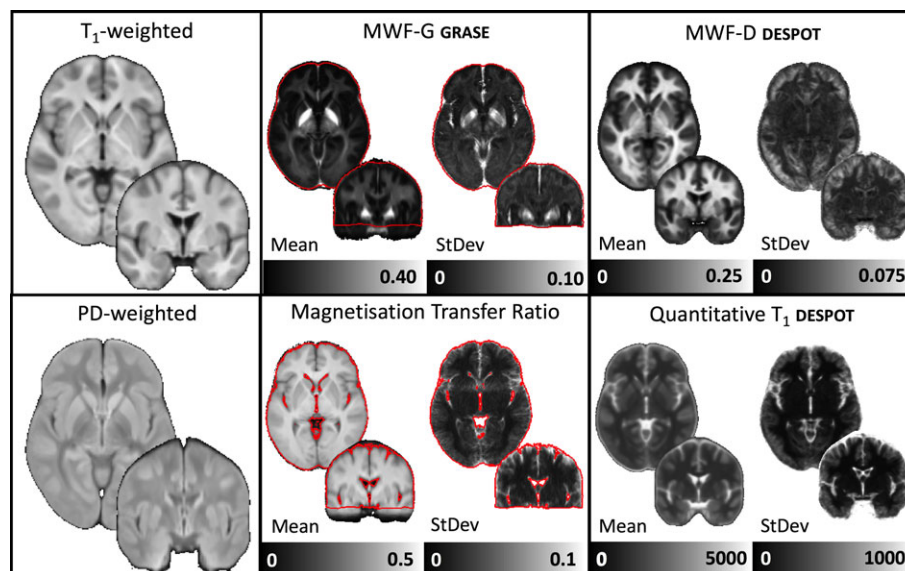


FIGURE 2 Population average images of the weighted and quantitative images for the healthy control cohort only. Red lines indicate the edge of coverage for all subjects in the myelin water fraction and magnetization transfer ratio images. Images are shown in MNI space on a coronal $Y = -2$ and an axial slice $Z = -2$ [Color figure can be viewed at wileyonlinelibrary.com]

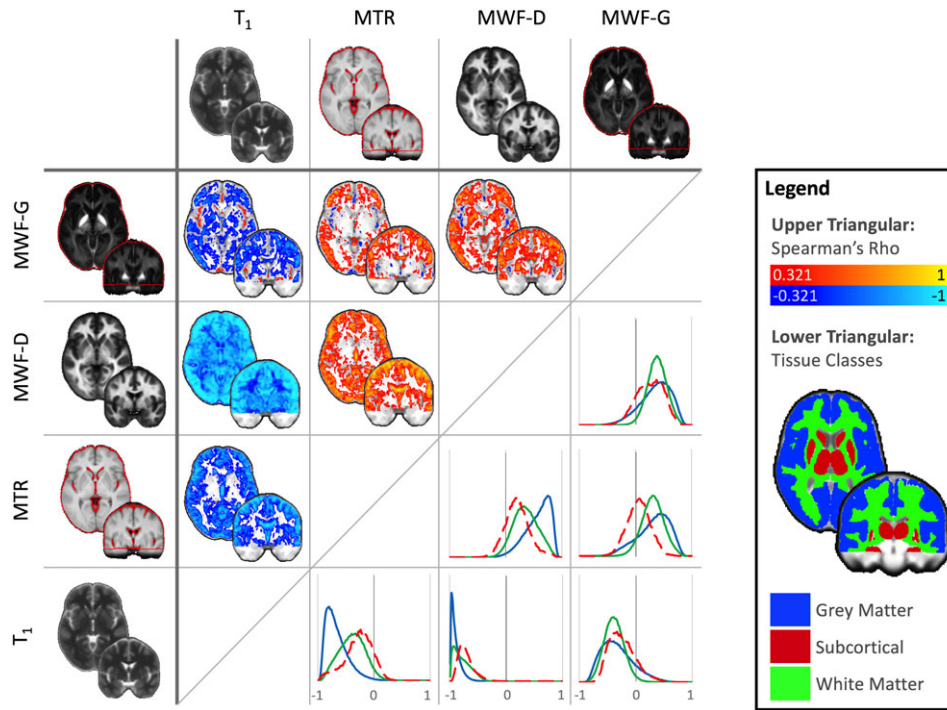


FIGURE 3 Cross-sectional Spearman's rank correlations between quantitative techniques, calculated for every voxel (upper triangular) in the healthy control cohort. Normalized histograms of the voxelwise correlations are also plotted according to tissue class (lower triangular, correlation coefficient value bins on the x-axis) with subcortical structures (red mask/dashed line), white matter (green mask/line), and gray matter (blue mask/line). Images are shown thresholded for visualization only at $\rho > 0.321$ or $\rho < 0.321$, $p < 0.05$ (two-tailed, uncorrected). Raw unthresholded volumes are available as supplementary material. Images are shown in MNI space on a coronal $Y = -2$ and an axial slice $Z = -2$ [Color figure can be viewed at wileyonlinelibrary.com]

performed in standard MNI space and only in areas of the brain with coverage in all four modalities.

3.1 | Correlations between techniques

To assess the similarity between methods at capturing individual differences, voxelwise Spearman rank correlations between parameters are demonstrated in Figure 3 (upper triangular). The histogram of the correlation values for four different tissue classes in healthy controls are in the lower triangular. The correlation maps shown in the upper triangle of Figure 3 are also provided in nifti format on neurovault (<https://neurovault.org/collections/4709/>) and at <https://www.msmpi.com/>.

Correlations across tissue classes (gray matter, WM, and subcortical gray structures) are reported in Table 3. These are reported separately for the healthy control population ($n = 38$) and the subset of

patients for whom all four modalities were available ($n = 24$). The correlation coefficients (ρ) are summarized in Table 3. The most consistent correlations across all tissue classes were found between MWF-D and qT_1 (median ρ across tissue classes 0.80, mean $\rho = 0.77$) and MWF-G and MWF-D (median $\rho = 0.59$, mean $\rho = 0.59$). In lesional tissue, for the 24 patients for whom all quantitative modalities were available, qMRI estimates covaried between all pairs of methods.

3.2 | MS and healthy control comparisons

Violin plots were created for each tissue class (gray matter, WM, and subcortical structures) in the patient and control groups (Figure 4a), indicating the spread of values for each region. In these analyses, all available data in the patient group was used ($n = 24$ for MTR, and $n = 56$ for the other methods). For all methods, significant differences

TABLE 3 Pearson's correlation coefficients between average quantitative values across subjects in different tissue classes

Modality		Controls (N = 38)				Patients (N = 24)				
						Normal appearing			Pathological	
1	2	GM	WM	Subcortical	GM	WM	Subcortical	Lesion	Perilesion	
MWF-G	QT1	-0.24 *	-0.51	-0.09	-0.19 *	-0.71 *	-0.57 *	-0.66 *	-0.64	
MWF-G	MWF-D	* 0.53	* 0.57	* 0.51	0.50 *	0.69 *	0.62 *	0.66 *	* 0.63	
MWF-G	MTR	0.23 *	0.54	-0.26	0.07	0.41	-0.10 *	0.57	0.48	
MWF-D	MTR	* 0.60	0.35	-0.11	* 0.54	0.25	0.17 *	0.54	0.37	
MWF-D	QT1	* -0.71	* -0.65	* -0.56	* -0.79	* -0.81	* -0.80	* -0.97	* -0.93	
MTR	QT1	* -0.90	-0.40	-0.14	* -0.87	-0.44	-0.42 *	-0.54	-0.39	

WM, white matter; GM, gray matter. Asterisk indicates $p < 0.01$

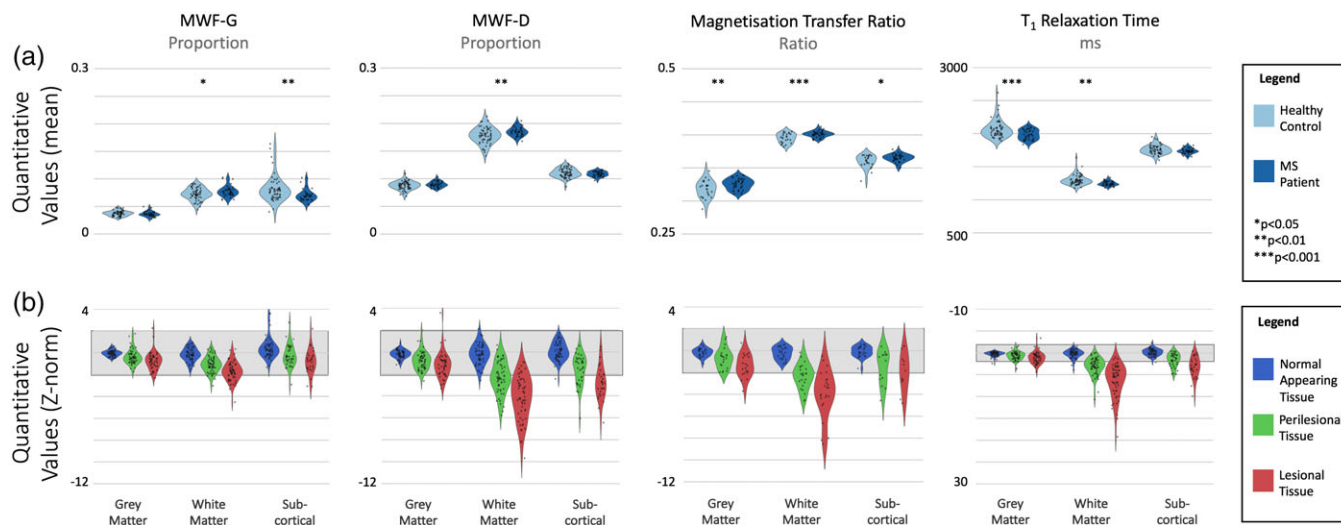


FIGURE 4 Top row (a): Average quantitative MRI values in three tissue classes for healthy controls and patients (normal appearing tissue only); and bottom row (b): The relative difference (Z scaled to the control sample, with control range indicated in gray) in individual patients in the three tissue classes according to whether the tissue is normal appearing, perilesional or lesional. In this part of the figure, the shaded area represents ± 2 standard deviations of the healthy control population values. Note the larger scale on the y-axis for T1 relaxation time [Color figure can be viewed at wileyonlinelibrary.com]

between MS and controls were detectable between mean quantitative values in WM regions ($p < 0.05$, corrected for multiple comparisons). Notably, these summary values for each tissue type explicitly excluded tissue identified as lesional and peri-lesional on clinical inspection. Figure 4b illustrates single subject Z-scores for patients compared to the healthy control template. There was extensive overlap with the control average in the patient average for NAWM. Lesional and perilesional tissue had lower MWF-D, MWF-G, and MTR, and higher qT_1 values, than the control average in lesional tissue for almost every individual patient. Similarly, Figure 5 demonstrates violin plots broken down into eight WM tracts. For both Figures 4

and 5, for healthy controls $N = 38$ for all metrics, while for MS patients $N = 56$ for MWF-G, MWF-D, and qT_1 ; and $N = 24$ for MTR (see Table 1 for subject demographics).

3.3 | AUC analysis

To quantify the relative sensitivity and specificity of the four quantitative MR techniques for detecting lesions, we calculated ROC curves for each individual patient. True positives were defined using the lesion masks, identified semi-automatically with radiologist supervision. A nonparametric Friedman test indicated that the AUCs for

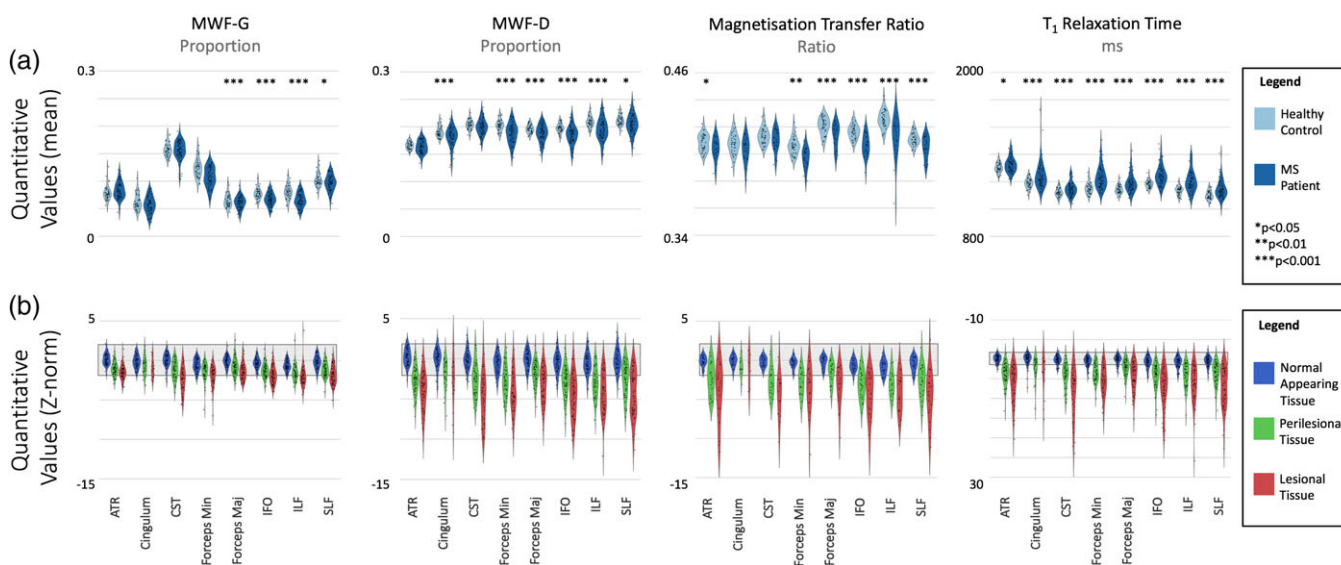


FIGURE 5 Top row (a): Average quantitative MRI values in eight white matter tracts (normal appearing tissue only); and bottom row (b): The relative difference (Z scaled to the control sample, with control range indicated in gray) in individual patients in the eight white matter tracts according to whether the tissue is normal appearing, perilesional or lesional. In this part of the figure, the shaded area represents ± 2 standard deviations of the healthy control population values. ATR, anterior thalamic radiation; CST, corticospinal tract; IFO, inferior fronto-occipital fasciculus; ILF, inferior longitudinal fasciculus; SLF, superior longitudinal fasciculus [Color figure can be viewed at wileyonlinelibrary.com]

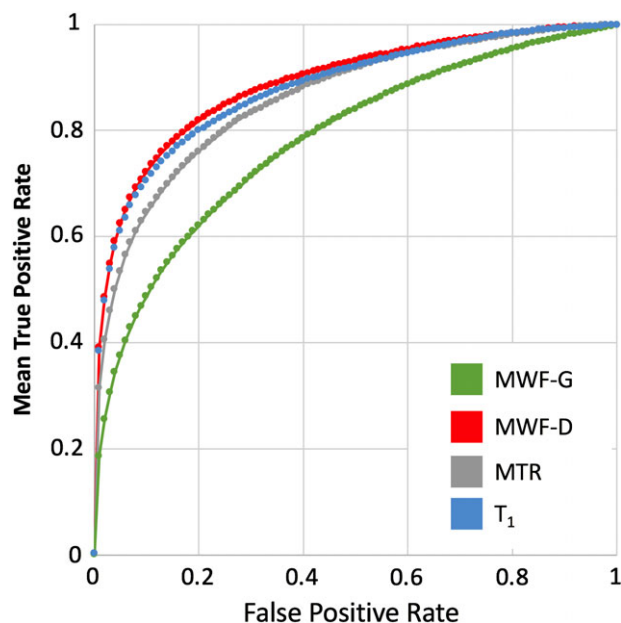


FIGURE 6 Receiver operator characteristic (ROC) curves for each quantitative MRI method showing accuracy of detecting manually labeled lesions by measuring voxel-level difference from controls (Z-score). Curves represent average true positive rates for fixed false positive rate values across the sub-sample of 24 patients with MS (only patients with all 4 MRI [$n = 24$] modalities available were included in this analysis) [Color figure can be viewed at wileyonlinelibrary.com]

detecting these delineated lesions were significantly different between the four quantitative MR techniques ($\chi^2 = 32.350$, $df = 3$, $p < 0.001$). Post hoc Wilcoxon signed rank tests (for paired data) indicated that MWF-G had a significantly lower performance than all other methods ($p < 0.001$) and MWF-D performed significantly better than qT_1 ($p = 0.017$). MWF-D had significantly higher AUC compared to both qT_1 ($p = 0.014$) and MTR ($p = 0.024$). There was no significant difference between qT_1 and MTR ($p = 0.92$). See Figure 6 for a plot of the ROC curves for each modality averaged over subjects. In this plot, each false discovery rate is fixed at the average (Fawcett, 2006). Importantly, the range of AUC values for MTR, qT_1 , and MWF-G were only slightly (albeit significantly and consistently) different (see Figure 6 for average ROCs at fixed false positive rate thresholds). Table 4 has summary statistics of the AUC measures per modality.

3.4 | Sample quantitative imaging parameter summary maps and brain coverage

In place of estimating statistical power for a limited amount of study designs/effect sizes, we include group average mean and SD maps of each parameter for the healthy control group (Figure 2) and

TABLE 4 Summary of area under the curve (AUC) values for each technique

	Mean AUC (SD)	Range (min, max)
MWF-G	0.78 (0.12)	(0.46, 0.94)
MWF-D	0.89 (0.08)	(0.65, 0.97)
MTR	0.86 (0.10)	(0.58, 0.96)
T_1	0.88 (0.08)	(0.61, 0.97)

provided as files in nifti format on neurovault (<https://neurovault.org/collections/4709/>) and at <https://www.msrmri.com/>. These summary statistics were calculated in MNI space.

4 | DISCUSSION

In this work, we have quantified the in vivo relationship between four advanced quantitative MRI techniques each putatively related to myelin. Metrics calculated from each of these techniques (MWF-G, MWF-D, MTR, and qT_1) showed strong relationships throughout the brain, though these relationships varied in different tissue types. The measures were all sensitive to differences in MS tissue compared to healthy controls, though to varying degrees, and had similar sensitivity profiles to manually identified MS lesions, with MWF-D being the most accurate. The strong associations between MWF-D and qT_1 observed in the present study have been demonstrated previously by (De Santis et al., 2014), albeit using a region-of-interest based approach and looking at average values across subjects. Indeed, if any measure is specific to myelin, it should also show close correspondence to T_1 in healthy tissue (Stüber et al., 2014).

However, in the MS brain specifically, the combination of increased water content, demyelination, and tissue iron deposition may disrupt this relationship. In the extreme case of completely demyelinated tissue, the inverse relationship between myelin and T_1 would break down as the MWF maps will approach zero. Correlation coefficients between MWF-D and MWF-G indicated a moderate correlation in most tissue types. In fact, after MWF-D and qT_1 , MWF-D and MWF-G were the pairs of measures significantly correlated across the most tissue classes. We observed weak, nonsignificant correlations in most tissue classes between MWF-D and MTR. Similar to all other inter-method comparisons, the correlation was significant in lesional tissue, indicating that although the methods may be measuring different quantities in healthy tissue, they are similarly sensitive in MS lesions.

There is a more established history in quantifying the similarity between MWF-G, MTR, and qT_1 . Previous results have demonstrated a lack of correlation between MWF-G and MTR in nonlesional WM (Vavasour et al., 2011). In an experimental autoimmune encephalomyelitis (EAE) guinea pig model, Gareau et al. (2000) suggested MTR was sensitive to inflammatory-related changes to the structure of WM whereas MWF-G was related to myelin content itself. They detected no relationship between MTR and MWF-G. Here, we detected a positive relationship on average in healthy control WM and in lesional tissue in MS patients. In the MS patient group, NAWM did have a positive though nonsignificant relationship indicating here in patients ($n = 24$), and maybe the Gareau investigation ($n = 24$ as well), there may simply have been insufficient samples to detect weak relationships. Several in vivo studies suggest that MTR is most strongly influenced by water content (Fox et al., 2005; Giacomini et al., 2009; Vavasour et al., 2011; Van Waesberghe et al., 1997). In the present study, we find weak correlations between MTR and qT_1 (which is strongly linked to water content) in WM, but similar to previous studies, we find a strong correlation in lesions, most likely due to an increase in water content.

In addition to characteristic focal lesions, there are diffuse abnormalities in the MS brain and notably: differences in brain volume (Stefano et al., 2010); increased edema (Filippi et al., 2012) and axonal swelling (Fisher et al., 2007); and diffuse changes in WM, as observed in the present study (Figures 4 and 5). We observed moderate global differences in the myelin-related measures between controls and our MS cohort (Figure 4), similarly to previous studies (Kitzler et al., 2012; Faizy et al., 2016; Kolind et al., 2012; Oh, Han, Lee, Nelson, & Pelletier, 2007; Cercignani, Bozzali, Iannucci, Comi, & Filippi, 2001; Vavasour et al., 1998). When looking at smaller WM tracts, all MR measurements in the present study showed differences between subjects with MS and healthy controls in at least some regions (Figure 5). Comparing MS to controls, qT_1 showed the highest number of significantly different regions (8), followed by MWF-D and MTR (6), and then MWF-G (4). These alterations in normal-appearing tissue may reflect diffuse alterations in the WM. Multi-component relaxation especially may be sensitive to subtle lesions that may be missed by radiological inspection (Laule et al., 2004). Additionally, cortical lesions may have downstream functional or structural effects on connected gray and WM tissue (Siffrin, Vogt, Radbruch, Nitsch, & Zipp, 2010). These nonlesional pathological features are likely represented in the performance curves of the modalities for lesion detection by apparently false positives (Figure 6). Cortical lesions are notoriously difficult to detect with both conventional and quantitative MRI (Calabrese & Castellaro, 2017), although with specific sequences, high field imaging, and ideally retrospective histopathological knowledge of lesion location, myelin content of cortical lesions can be investigated by mapping the lesions detected with these advanced techniques onto myelin-sensitive MRI (Jonkman et al., 2016)] maps; unfortunately, none of these methods were available for this study.

One crucial aspect of individual differences relevant here is the effect of age on all of the quantities. Changes in WM tissue content occur throughout the lifespan (Callaghan et al., 2014) and, if investigating single patients, this change needs to be taken into account. In this study, we used an average and *SD* taken from a sample of healthy individuals with a wide age-range, from 20 to 52 years. This is not ideal. MS can occur at any point throughout the lifespan and therefore detecting lesions or abnormalities needs to be performed in the context of the maturation of the brain at the time of the scan. What is still missing is a measure of each quantity appropriate to age, akin to a growth curve, though this has been developed in younger cohorts (Dean III et al., 2014; Sadeghi et al., 2013).

All quantitative MR measurements showed differences between lesions and NAWM. Compared to radiologist-detected lesions, MWF-D had the best performance in detecting these lesions (Figure 6), followed by qT_1 and MTR. Good performance by qT_1 , in particular, is predictable since the presence of lesions on PD/ T_2 -weighted images is due to their increase in water content, and qT_1 is greatly influenced by water content. Lesions identified by MWF-G were the least similar to radiologist-detected lesions. This could be because MWF-G is only moderately correlated with water content ($r = -0.36$; Vavasour et al., 2011), and it is known that not all lesions show demyelination (Van Der Valk & De Groot, 2000).

ROC curves are used here as an indicator of *relative* sensitivity and specificity of the MRI methods, but their values can be misleading

when the true positive/true negative ratio is very skewed, as is the case here. Lesion volumes were, on average, about 0.5% of the total WM volume mask used in this analysis. With these proportions, a 1% false positive rate could have twice as many false positive voxels as there are lesional voxels, even with perfect sensitivity (100 true positive rates). To improve on this, many studies have combined multiple image modalities, both qualitative and quantitative, to produce more accurate lesion segmentations (Brosch et al., 2016; Lladó et al., 2012; Mah, Jager, Kennard, Husain, & Nachev, 2014). Notably, combined analysis of MWF-G and MTR over time has shown promise in distinguishing tissue injury and remyelination (McCreary et al., 2009).

ROC curves also miss another important factor in profiling tissue biomarkers in MS. Changes in both myelin and water content are known to occur (Laule et al., 2004), reflecting different aspects of the pathological processes. To accurately separate these features, any given technique should preferably be sensitive to one or the other, to distinguish which process is taking place. From this point of view, it is apparent here that qT_1 is very sensitive to tissue changes (e.g., larger *z* scores than any other method in Figures 4 and 5) but not specific to which change is occurring in the tissue, for example, change in water content or myelin, reflected in the lower area under the curve in Figure 6 compared to MWF-D. With the advantages and disadvantages of each technique, it is also necessary to consider the relative performance of each technique with regards to the acquisition time. The voxel volume for all sequences was $\sim 5 \text{ mm}^3$, with isotropic voxels and whole-head coverage for mcDESPOT, whereas GRASE and MTR data were collected with 5 mm thick slices and limited coverage. With respect to time, GRASE has a disadvantage compared to mcDESPOT and MTR. GRASE is fundamentally limited by the need to acquire a sufficient number of data points in the T_2 -decay, here 32 points going out to 320 ms, and a sufficiently long TR, in this study $TR = 1,000 \text{ ms}$, to avoid T_1 -weighting confounds, although recent developments may allow faster GRASE acquisition (Chen, Majumdar, & Kozłowski, 2014; Zhang et al., 2015). Sensitivity to tissue-specific changes as well as acquisition time should be taken into account when selecting the appropriate quantitative technique to use in a study.

This brings up another methodological limitation when comparing the different methods. Limitations on matching image resolution across acquisitions mean that voxels can have different aspects of partial volume to each other. Therefore, while MWF-D and qT_1 are matched on voxel dimensions and are acquired in the same space, MWF-G and MTR are highly anisotropic in the slice dimension. This is a risk, especially when investigating the association's voxelwise. In areas such as the ventricles (where there is strong partial volume in the inferior–superior axis), this could falsely induce or occlude associations between methods. Although spatial smoothing may help, matching acquisition dimensions can better address the problem. In addition, the fact that the mcDESPOT acquisition was used for non-linear registration means that errors in registration are less likely for qT_1 and MWF-D compared to the other two methods where an additional rigid registration is needed and error may be introduced just to MTR and MWF-G due to the compound registration approach. In all cases however, multiple interpolation steps were avoided by combining the calculated transformations and interpolating from native to MNI space in a single step.

In summary, we demonstrate that individual differences of WM tissue content are not consistent between WM quantification techniques in the same individuals. Although important in itself, this is especially important as these techniques are being used more and more in research, referred to interchangeably, though they are obviously quite different. These techniques are also being increasingly used in clinical trials of WM disorders and, where pathological tissue is concerned, we show reassuringly good correspondence between the techniques. However, depending on the exact purpose of a study, one technique may be preferred over another. For studies that require the greatest confidence in the interpretation of results as changes specific to myelin, MWF-G has undergone the greatest degree of validation and is thought to provide the greatest specificity. If sensitivity to differences in tissue types (e.g., lesion vs. NAWM, NAWM vs. healthy control WM) is more important than the strictest specificity, MWF-D and qT1 showed the greatest separation. Consequently, these techniques are the most likely to be sensitive to change over time. If acquisition or analysis times are severely limited, MTR or qT1 provide the most practical tools. To enable bespoke power analyses for future trials and studies, we provide voxelwise estimates of the sample mean and SD of the four quantitative MRI techniques (<https://neurovault.org/collections/4709/>).

ACKNOWLEDGMENTS

Sincere thanks to our volunteers and their families, the MRI technologists, staff at the UBC MRI Research Centre, Yinshan Zhao for statistical discussion, and MSMRI (specifically Ken Bigelow, Andrew Riddehough, and Vilmos Soti) for computing support. We thank Philips Healthcare for their ongoing support. Jonathan O'Muircheartaigh is supported by a Sir Henry Dale Fellowship jointly funded by the Wellcome Trust and the Royal Society (Grant Number 206675/Z/17/Z). This work was supported by the Wellcome Trust/EPSCRC Centre for Medical Engineering [WT 203148/Z/16/Z]. The study was sponsored by F. Hoffman-La Roche AG. Authors Victoria Levesque, Hideki Garren, and David Clayton are employees of Genentech Inc. Genentech (owned by F. Hoffmann-La Roche) sponsored the collection of the data used in this study. Shannon Kolind has received research support and consulting fees from F. Hoffmann La Roche and Sanofi Genzyme, and is supported by the Milan & Maureen Ilich Foundation as well as the Michael Smith Foundation for Health Research (Scholar Award). Anthony Traboulsee has research funding from Chugai, Roche, Novartis, Genzyme, Biogen as well as consultancy honoraria from Genzyme, Roche, Teva, Biogen, Serono. Emil Ljungberg is in receipt of a PhD studentship jointly funded by General Electric (GE) Healthcare and the National Institute for Health Research (NIHR) Biomedical Research Centre at South London and Maudsley NHS Foundation Trust and King's College London. Alexander Rauscher is supported by Canada Research Chairs and has received speaker fees from Philips. Roger Tam has provided technical support for clinical trials sponsored by Roche and Sanofi Genzyme, for which he received indirect research funding support. David Li has received research funding from the Canadian Institute of Health Research and Multiple Sclerosis Society of Canada. He is the Emeritus Director of the UBC MS/MRI Research Group which has been contracted to perform central analysis of MRI scans for therapeutic trials

with Novartis, Perceptives, Roche, and Sanofi-Aventis. He has acted as a consultant to Vertex Pharmaceuticals and served on the Data and Safety Advisory Board for Opexa Therapeutics and Scientific Advisory Boards for Adelphi Group, Celgene, Novartis, and Roche. He has also given lectures which have been supported by nonrestricted education grants from Academy of Health Care Learning, Biogen-Idec, Consortium of MS Centers, Novartis, Sanofi-Genzyme, and Teva. The UBC MS/MRI Research Group has also received grant support for investigator-initiated independent studies from Genzyme, Merck-Serono, Novartis, and Roche.

ORCID

Jonathan O'Muircheartaigh  <https://orcid.org/0000-0002-8033-6959>

Emil Ljungberg  <https://orcid.org/0000-0003-1456-7967>

REFERENCES

- Alexander, A. L., Hurley, S. A., Samsonov, A. A., Adluru, N., Hosseinbor, A. P., Mossahebi, P., ... Field, A. S. (2011). Characterization of cerebral white matter properties using quantitative magnetic resonance imaging stains. *Brain Connectivity*, *1*, 423–446.
- Avants, B. B., Epstein, C. L., Grossman, M., & Gee, J. C. (2008). Symmetric diffeomorphic image registration with cross-correlation: Evaluating automated labeling of elderly and neurodegenerative brain. *Medical Image Analysis*, *12*, 26–41.
- Avants, B. B., Tustison, N. J., Song, G., Cook, P. A., Klein, A., & Gee, J. C. (2011). A reproducible evaluation of ANTs similarity metric performance in brain image registration. *NeuroImage*, *54*, 2033–2044.
- Barkhof, F., Calabresi, P. A., Miller, D. H., & Reingold, S. C. (2009). Imaging outcomes for neuroprotection and repair in multiple sclerosis trials. *Nature Reviews. Neurology*, *5*, 256–266.
- Brosch, T., Tang, L., Yoo, Y., Li, D., Traboulsee, A., & Tam, R. (2016). Deep 3D convolutional encoder networks with shortcuts for multiscale feature integration applied to multiple sclerosis lesion segmentation. *IEEE Transactions on Medical Imaging*, *35*, 1229–1239.
- Calabrese, M., & Castellaro, M. (2017). Cortical gray matter MR imaging in multiple sclerosis. *Neuroimaging Clinics of North America*, *27*, 301–312.
- Callaghan, M. F., Freund, P., Draganski, B., Anderson, E., Cappelletti, M., Chowdhury, R., ... Weiskopf, N. (2014). Widespread age-related differences in the human brain microstructure revealed by quantitative magnetic resonance imaging. *Neurobiology of Aging*, *35*, 1862–1872.
- Cercignani, M., Bozzali, M., Iannucci, G., Comi, G., & Filippi, M. (2001). Magnetisation transfer ratio and mean diffusivity of normal appearing white and grey matter from patients with multiple sclerosis. *Journal of Neurology, Neurosurgery, and Psychiatry*, *70*, 311–317.
- Chen, H. S., Majumdar, A., & Kozlowski, P. (2014). Compressed sensing CPMG with group-sparse reconstruction for myelin water imaging. *Magnetic Resonance in Medicine*, *71*, 1166–1171.
- Cox, R. W. (1996). AFNI: Software for analysis and visualization of functional magnetic resonance neuroimages. *Computers and Biomedical Research*, *29*, 162–173.
- De Santis, S., Drakesmith, M., Bells, S., Assaf, Y., & Jones, D. K. (2014). Why diffusion tensor MRI does well only some of the time: Variance and covariance of white matter tissue microstructure attributes in the living human brain. *NeuroImage*, *89*, 35–44.
- Dean, D. C., III, O'Muircheartaigh, J., Dirks, H., Waskiewicz, N., Lehman, K., Walker, L., ... Deoni, S. C. L. (2014). Modeling healthy male white matter and myelin development: 3 through 60 months of age. *NeuroImage*, *84*, 742–752.
- Demšar, J. (2006). Statistical comparisons of classifiers over multiple data sets. *Journal of Machine Learning Research*, *7*, 1–30.
- Deoni, S. C. L. (2007). High-resolution T1 mapping of the brain at 3T with driven equilibrium single pulse observation of T1 with high-speed incorporation of RF field inhomogeneities (DESPOT1-HIFI). *Journal of Magnetic Resonance Imaging*, *26*, 1106–1111.

- Deoni, S. C. L. (2009). Transverse relaxation time (T2) mapping in the brain with off-resonance correction using phase-cycled steady-state free precession imaging. *Journal of Magnetic Resonance Imaging*, 30, 411–417.
- Deoni, S. C. L. (2011). Correction of Main and transmit magnetic Field (B0 and B1) inhomogeneity effects in multicomponent-driven equilibrium single-pulse observation of T1 and T2. *Magnetic Resonance in Medicine*, 65, 1021–1035.
- Deoni, S. C. L., & Kolind, S. H. (2015). Investigating the stability of mcDESPOT myelin water fraction values derived using a stochastic region contraction approach. *Magnetic Resonance in Medicine*, 73, 161–169.
- Deoni, S. C. L., Rutt, B. K., Arun, T., Pierpaoli, C., & Jones, D. K. (2008). Gleaning multicomponent T1 and T2 information from steady-state imaging data. *Magnetic Resonance in Medicine*, 60, 1372–1387.
- Faizy, T. D., Thaler, C., Kumar, D., Sedlacik, J., Broocks, G., Grosser, M., ... Siemonsen, S. (2016). Heterogeneity of multiple sclerosis lesions in multislice myelin water imaging. *PLoS One*, 11, 1–13.
- Fatouros, P. P., Marmarou, A., Kraft, K. A., Inao, S., & Schwarz, F. P. (1991). In vivo brain water determination by T1 measurements: Effect of total water content, hydration fraction, and Field strength. Article. *Magnetic Resonance in Medicine*, 17, 402–413.
- Fawcett, T. (2006). An introduction to ROC analysis. *Pattern Recognition Letters*, 27, 861–874.
- Filippi, M., Campi, a., Dousset, V., Baratti, C., Martinelli, V., Canal, N., ... Comi, G. (1995). A magnetization transfer imaging study of normal-appearing white matter in multiple sclerosis. *Neurology*, 45, 478–482.
- Filippi, M., Rocca, M. A., Barkhof, F., Brück, W., Chen, J. T., Comi, G., ... Lassmann, H. (2012). Association between pathological and MRI findings in multiple sclerosis. *Lancet Neurology*, 11, 349–360.
- Fisher, E., Chang, A., Fox, R. J., Tkach, J. A., Svarovsky, T., Nakamura, K., ... Trapp, B. D. (2007). Imaging correlates of axonal swelling in chronic multiple sclerosis brains. *Annals of Neurology*, 62, 219–228.
- Fox, R. J., Fisher, E., Tkach, J., Lee, J.-C., J a, C., & R a, R. (2005). Brain atrophy and magnetization transfer ratio following methylprednisolone in multiple sclerosis: Short-term changes and long-term implications. *Multiple Sclerosis (Houndmills, Basingstoke, England)*, 11, 140–145.
- Gareau, P. J., Rutt, B. K., Karlik, S. J., & Mitchell, J. R. (2000). Magnetization transfer and multicomponent T2 relaxation measurements with histopathologic correlation in an experimental model of MS. *Journal of Magnetic Resonance Imaging*, 11, 586–595.
- Gelman, N., Ewing, J. R., Gorell, J. M., Spickler, E. M., & Solomon, E. G. (2001). Interregional variation of longitudinal relaxation rates in human brain at 3.0 T: Relation to estimated iron and water contents. *Magnetic Resonance in Medicine*, 45, 71–79.
- Giacomini, P. S., Levesque, I. R., Ribeiro, L., Narayanan, S., Francis, S., Pike, G. B., & Arnold, D. L. (2009). Measuring demyelination and Remyelination in acute multiple sclerosis lesion voxels. *Archives of Neurology*, 66, 375–381.
- Harrison, D. M., Shiee, N., Bazin, P. L., Newsome, S. D., Ratchford, J. N., Pham, D., ... Reich, D. S. (2013). Tract-specific quantitative MRI better correlates with disability than conventional MRI in multiple sclerosis. *Journal of Neurology*, 260, 397–406.
- Hauser, S. L., Bar-Or, A., Comi, G., Giovannoni, G., Hartung, H. P., Hemmer, B., ... Traboulsee, A. (2017). Ocrelizumab versus interferon beta-1a in relapsing multiple sclerosis. *New England Journal of Medicine*, 376(3), 221–234.
- Hua, K., Zhang, J., Wakana, S., Jiang, H., Li, X., Reich, D. S., ... Mori, S. (2008). Tract probability maps in stereotaxic spaces: Analyses of white matter anatomy and tract-specific quantification. *NeuroImage*, 39, 336–347.
- Hurley SA, Mossahebi PM, Samsonov AA, Alexander AL, Deoni SC, Fisher R, Duncan ID, Field AS (2010). Multicomponent relaxometry (mcDESPOT) in the shaking pup model of dysmyelination. In: Proceedings of the 18th Meeting of the International Society for Magnetic Resonance in Medicine, Stockholm, p. 4516. http://cds.ismrm.org/protected/10MProceedings/files/4516_88.pdf.
- Jenkinson, M., & Smith, S. (2001). A global optimisation method for robust affine registration of brain images. *Medical Image Analysis*, 5, 143–156.
- Jonkman, L. E., Fleysher, L., Steenwijk, M. D., Koeleman, J. A., de Snoo, T.-P., Barkhof, F., ... Geurts, J. J. (2016). Ultra-high field MTR and qR2* differentiates subpial cortical lesions from normal-appearing gray matter in multiple sclerosis. *Multiple Sclerosis Journal*, 22, 1306–1314.
- Kamman, R. L., Go, K. G., Brouwer, W., & Berendsen, H. J. C. (1988). Nuclear magnetic resonance relaxation in experimental brain edema: Effects of water concentration, protein concentration, and temperature. *Journal of Magnetic Resonance in Medicine*, 6, 265–274.
- Kitzler, H. H., Su, J., Zeineh, M., Harper-Little, C., Leung, A., Kremenchutzky, M., ... Rutt, B. K. (2012). Deficient MWF mapping in multiple sclerosis using 3D whole-brain multi-component relaxation MRI. *NeuroImage*, 59, 2670–2677.
- Kolind, S., Matthews, L., Johansen-Berg, H., Leite, M. I., Williams, S. C. R., Deoni, S., & Palace, J. (2012). Myelin water imaging reflects clinical variability in multiple sclerosis. *NeuroImage*, 60, 263–270.
- Laule, C., Kozlowski, P., Leung, E., Li, D. K. B., MacKay, A. L., & Moore, G. R. W. (2008). Myelin water imaging of multiple sclerosis at 7T: Correlations with histopathology. *NeuroImage*, 40, 1575–1580.
- Laule, C., Leung, E., Li, D. K. B., Traboulsee, A. L., Paty, D. W., MacKay, A. L., & Moore, G. R. W. (2006). Myelin water imaging in multiple sclerosis: Quantitative correlations with histopathology. *Multiple Sclerosis*, 12, 747–753.
- Laule, C., Vavasour, I. M., Moore, G. R. W., Oger, J., Li, D. K. B., Paty, D. W., & MacKay, A. L. (2004). Water content and myelin water fraction in multiple sclerosis: A T 2 relaxation study. *Journal of Neurology*, 251, 284–293.
- Lladó, X., Oliver, A., Cabezas, M., Freixenet, J., Vilanova, J. C., Quiles, A., ... Rovira, À. (2012). Segmentation of multiple sclerosis lesions in brain MRI: A review of automated approaches. *Information Sciences*, 186, 164–185.
- MacKay, A., Laule, C., Vavasour, I., Bjarnason, T., Kolind, S., & Mädler, B. (2006). Insights into brain microstructure from the T2 distribution. *Magnetic Resonance Imaging*, 24, 515–525.
- MacKay, A. L., & Laule, C. (2016). Magnetic resonance of myelin water: an in vivo marker for myelin. *Brain Plasticity*, 2(1), 71–91.
- Mah, Y.-H., Jager, R., Kennard, C., Husain, M., & Nachev, P. (2014). A new method for automated high-dimensional lesion segmentation evaluated in vascular injury and applied to the human occipital lobe. *Cortex: A Journal of the Devoted to the Study of the Nervous System and Behavior*, 56, 51–63.
- Margaret Cheng, H. L., Stikov, N., Ghugre, N. R., & Wright, G. A. (2012). Practical medical applications of quantitative MR relaxometry. *Journal of Magnetic Resonance Imaging*, 36, 805–824.
- McAusland, J., Tam, R. C., Wong, E., Riddehough, A., & Li, D. K. (2010). Optimizing the use of radiologist seed points for improved multiple sclerosis lesion segmentation. *IEEE Transactions on Biomedical Engineering*, 57(11), 2689–2698.
- McCreary, C. R., Bjarnason, T. A., Skihar, V., Mitchell, J. R., Yong, V. W., & Dunn, J. F. (2009). Multiexponential T2 and magnetization transfer MRI of demyelination and remyelination in murine spinal cord. *NeuroImage*, 45, 1173–1182.
- Mezer, A., Yeatman, J. D., Stikov, N., Kay, K. N., Cho, N.-J., Dougherty, R. F., ... Wandell, B. A. (2013). Quantifying the local tissue volume and composition in individual brains with magnetic resonance imaging. *Nature Medicine*, 19, 1667–1672.
- Mottershead, J. P., Schmierer, K., Clemence, M., Thornton, J. S., Scaravilli, F., Barker, G. J., ... Miller, D. H. (2003). High field MRI correlates of myelin content and axonal density in multiple sclerosis: A post-mortem study of the spinal cord. *Journal of Neurology*, 250, 1293–1301.
- Oh, J., Han, E. T., Lee, M. C., Nelson, S. J., & Pelletier, D. (2007). Multislice brain myelin water fractions at 3T in multiple sclerosis. *Journal of Neuroimaging*, 17, 156–163.
- Ontaneda, D., Thompson, A. J., Fox, R. J., & Cohen, J. A. (2016). Progressive multiple sclerosis: Prospects for disease therapy, repair, and restoration of function. *The Lancet*, 6736, 1–10.
- Prasloski, T., Mädler, B., Xiang, Q. S., MacKay, A., & Jones, C. (2012). Applications of stimulated echo correction to multicomponent T2 analysis. *Magnetic Resonance in Medicine*, 67, 1803–1814.
- Prasloski, T., Rauscher, A., MacKay, A. L., Hodgson, M., Vavasour, I. M., Laule, C., & Mädler, B. (2012). Rapid whole cerebrum myelin water imaging using a 3D GRASE sequence. *NeuroImage*, 63, 533–539.
- Rooney, W. D., Johnson, G., Li, X., Cohen, E. R., Kim, S. G., Ugurbil, K., & Springer, C. S. (2007). Magnetic field and tissue dependencies of

- human brain longitudinal 1H₂O relaxation in vivo. *Magnetic Resonance in Medicine*, 57, 308–318.
- Sadeghi, N., Prastawa, M., Fletcher, P. T., Wolff, J., Gilmore, J. H., & Gerig, G. (2013). Regional characterization of longitudinal DT-MRI to study white matter maturation of the early developing brain. *NeuroImage*, 68, 236–247.
- Schmierer, K., Scaravilli, F., Altmann, D. R., Barker, G. J., & Miller, D. H. (2004). Magnetization transfer ratio and myelin in postmortem multiple sclerosis brain. *Annals of Neurology*, 56, 407–415.
- Schmierer, K., Tozer, D. J., Scaravilli, F., Altmann, D. R., Barker, G. J., Tofts, P. S., & Miller, D. H. (2007). Quantitative magnetization transfer imaging in postmortem multiple sclerosis brain. *Journal of Magnetic Resonance Imaging*, 26, 41–51.
- Siffrin, V., Vogt, J., Radbruch, H., Nitsch, R., & Zipp, F. (2010). Multiple sclerosis – Candidate mechanisms underlying CNS atrophy. *Trends in Neurosciences*, 33, 202–210.
- Stefano, N. D., Giorgio, A., Battaglini, M., Rovaris, M., Sormani, M. P., Barkhof, F., ... Filippi, M. (2010). Assessing brain atrophy rates in a large population of untreated multiple sclerosis subtypes. *Neurology*, 74, 1868–1876.
- Stüber, C., Morawski, M., Schäfer, A., Labadie, C., Wähner, M., Leuze, C., ... Turner, R. (2014). Myelin and iron concentration in the human brain: A quantitative study of MRI contrast. *NeuroImage*, 93, 95–106.
- Tam, R. C., Traboulsee, A., Riddehough, A., Sheikhzadeh, F., & Li, D. K. B. (2011). The impact of intensity variations in T1-hypointense lesions on clinical correlations in multiple sclerosis. *Multiple Sclerosis*, 17, 949–957.
- Van Der Valk, P., & De Groot, C. J. A. (2000). Staging of multiple sclerosis (MS) lesions: Pathology of the time frame of MS. *Neuropathology and Applied Neurobiology*, 26, 2–10.
- Van Waesberghe, J. H. T. M., Castelijns, J. A., Scheltens, P., Truyen, L., Lycklama À Nijeholt, G. J., Hoogenraad, F. G., ... Barkhof, F. (1997). Comparison of four potential MR parameters for severe tissue destruction in multiple sclerosis lesions. *Magnetic Resonance Imaging*, 15, 155–162.
- Van Waesberghe, J. H. T. M., Kamphorst, W., De Groot, C. J. A., Van Walderveen, M. A. A., Castelijns, J. A., Ravid, R., ... Barkhof, F. (1999). Axonal loss in multiple sclerosis lesions: Magnetic resonance imaging insights into substrates of disability. *Annals of Neurology*, 46, 747–754.
- Vavasour, I. M., Laule, C., Li, D. K. B., Traboulsee, A. L., & MacKay, A. L. (2011). Is the magnetization transfer ratio a marker for myelin in multiple sclerosis? *Journal of Magnetic Resonance Imaging*, 33, 713–718.
- Vavasour, I. M., Whittall, K. P., MacKay, A. L., Li, D. K. B., Vorobeychik, G., & Paty, D. W. (1998). A comparison between magnetization transfer ratios and myelin water percentages in normals and multiple sclerosis patients. *Magnetic Resonance in Medicine*, 40, 763–768.
- Whittall, K. P., & MacKay, A. L. (1989). Quantitative interpretation of NMR relaxation data. *Journal of Magnetic Resonance (1969)*, 84, 134–152.
- Wood, T. C., Simmons, C., Hurley, S. A., Vernon, A. C., Torres, J., Dell'Acqua, F., ... Cash, D. (2016). Whole-brain ex-vivo quantitative MRI of the cuprizone mouse model. *PeerJ*, 4, e2632.
- Yoo, Y., Prasloski, T., Vavasour, I., MacKay, A., Traboulsee, A. L., Li, D. K. B., & Tam, R. C. (2015). Fast computation of myelin maps from MRI T2 relaxation data using multicore CPU and graphics card parallelization. *Journal of Magnetic Resonance Imaging*, 41, 700–707.
- Zhang, J., Vavasour, I., Kolind, S., Baumeister, B., Rauscher, A., MacKay, A. (2015). *Advanced myelin water imaging techniques for rapid data acquisition and long T2 component measurements*. In: Proceedings of the International Society for Magnetic Resonance in Medicine, Concord, CA. p. 0824.

How to cite this article: O'Muircheartaigh J, Vavasour I, Ljungberg E, et al. Quantitative neuroimaging measures of myelin in the healthy brain and in multiple sclerosis. *Hum Brain Mapp.* 2019;40:2104–2116. <https://doi.org/10.1002/hbm.24510>